A comparison of direct and iterative methods for determining traction-separation relations

Shravan Gowrishankar, Haixia Mei, Kenneth M. Liechti & Rui Huang

International Journal of Fracture

ISSN 0376-9429
Volume 177
Number 2

Int J Fract (2012) 177:109-128
DOI 10.1007/s10704-012-9758-3

Springer

Int J Fract (2012) 177:109–128
DOI 10.1007/s10704-012-9758-3

ORIGINAL PAPER

A comparison of direct and iterative methods for determining traction-separation relations

Shravan Gowrishankar · Haixia Mei · Kenneth M. Liechti · Rui Huang

Received: 5 May 2012 / Accepted: 20 July 2012 / Published online: 10 August 2012

Abstract Traction-separation relations have been used to represent the adhesive interactions at bimaterial interfaces for contact and fracture analyses. There are a variety of methods for determining these relations, which are broadly sorted into iterative and direct methods. Here we compare the traction-separation relations for a silicon/epoxy interface extracted by two such methods. Interferometric measurements of the normal crack opening displacements near the crack front in a double-cantilever beam specimen were exploited along with an augmented analytical solution for J-integral as an illustration of the direct method. As an example of the iterative method, we relied on comparisons of measured crack length and normal crack opening displacements with numerical simulations obtained from two types of candidate traction-separation relations. It was found that the shape of the traction-separation relation, in addition to the interfacial toughness and strength, was needed to bring the numerical solutions into optimal registration with the measurements. On the other hand, the direct method lived up to its name in terms of ease of parameter extraction while providing a reasonable set of parameters.

S. Gowrishankar · H. Mei · K. M. Liechti (✉) · R. Huang
Department of Aerospace Engineering and Engineering Mechanics, Center for Mechanics of Solids, Structures and Materials, The University of Texas at Austin, Austin, TX 78712, USA
e-mail: kml@mail.utexas.edu

Keywords Interface fracture · Infrared crack opening interferometry · Traction-separation relations · Silicon/epoxy interface

1 Introduction

Laminated structures are ubiquitous in several industries including aerospace, naval, automobile and microelectronics. Technological advances have led to the introduction of new materials and processes with particularly short lead times. At the same time, mechanical reliability is paramount, and durability prediction is an attractive alternative to extensive testing. The current approach to characterizing the durability of the interfaces in layered structures is often by way of linear elastic fracture mechanics (Hutchinson and Suo 1991). However, limitations to this approach can arise, especially for interfaces between thin layers and materials with inelastic properties. The cohesive zone model, first proposed by Dugdale (1960) and Barenblatt (1962) in order to describe the near crack tip behavior, has gained popularity in recent years for modeling crack nucleation and propagation. Cohesive zone models have been effective in modeling not only interfacial delamination as shown by many groups (Feraren and Jensen 2004; Parmigiani and Thouless 2007; Li et al. 2005; Valoroso and Champaney 2006), but also a plethora of other interface problems such as crack nucleation at bi-material corners (Mohammed and Liechti 2000), plastic dissipation

in thin debonding films (Shirani and Liechti 1998), and delamination of composites (Li and Thouless 2006; Moroni and Pirondi 2011; Sørensen and Jacobsen 2003; Li et al. 2005). However, cohesive zone models require specific material parameters in order to make meaningful predictions. In addition, the criteria for mixed-mode damage initiation and fracture must be determined, which may then be used to simulate mode-dependent fracture processes (Högberg et al. 2007; Li and Thouless 2006; Parmigiani and Thouless 2007; Zhu et al. 2009).

In order to obtain the material parameters required for the cohesive zone model, one of the most commonly used specimens is the double cantilever beam (DCB) specimen (Kanninen 1973; Williams 1989; Swadener et al. 1999; Zhu et al. 2009). The main advantage of using the DCB specimen is that a nominally mode-I loading can be applied to the crack, which allows the mode-I toughness of the interface to be measured. However, the DCB specimen can also be used with an uneven bending moment or loaded in an asymmetric manner in order to measure mixed-mode fracture properties (Sørensen and Kirkegaard 2006).

No matter which specimen is used, a local measurement such as the crack opening displacement near the crack tip is required for extracting the traction-separation relation in the cohesive zone model. Interferometry has been widely used to characterize crack tip behavior in glass/adhesive systems (Chai and Liechti 1992; Mello and Liechti 2006) and in thin film blister tests (Shirani and Liechti 1998). Naturally, the use of interferometry is restricted to the materials transparent to the light source. In this work, the silicon/epoxy system was characterized using interferometry with infrared (IR) light because of the IR transparency of silicon.

The extraction of traction-separation relations is generally approached in one of the two ways: a direct method and an iterative method. The direct method, as demonstrated by many groups (Sørensen and Jacobsen 2003; Sorensen et al. 2008; Zhu et al. 2009), delivers results based mainly on measured displacements without recourse to extensive numerical analysis. However, the extraction of traction-separation relations through the direct method can be constrained by resolution issues in locating the crack front and measuring the crack opening displacements. The iterative method, on the other hand, determines parameters by comparing numerical solutions and measurements, which has been frequently employed in the past (Cox and Marshall 1991; Li et al. 2005; Mello and Liechti 2006; Sorensen et al. 2008).

This paper explores the determination of the traction-separation relations of the silicon/epoxy interface using both methods. The direct method combined infra-red crack opening interferometry (IR-COI) measurements with an augmented analytical solution for J-integral to extract the traction-separation relation. Next, an iterative method was adopted to compare the same measurements with finite element simulations using two types of candidate traction-separation relations. The results from the two methods are compared to conclude with remarks on their effectiveness and limitations.

2 Experiment

In this section, we describe the procedures that were developed to fabricate DCB specimens and then fracture them in a wedge test configuration while making measurements of normal crack opening displacements (NCOD) using IR-COI.

2.1 Sample preparation

A schematic of specimen geometry and apparatus is shown in Fig. 1. The specimen consists of two silicon strips joined by a layer of epoxy. The n-type Si (111) wafers used here were polished on both sides to allow the use of IR-COI and were obtained from WRS Materials. The wafers were 50 mm in diameter and nominally 280 μm in thickness. Although silicon wafers can be cut in various directions, the Si (111) is preferred because the (111) plane has the smoothest surface and presents the most dense arrangement of atoms on the surface. An automatic dicer (Disco, model DAD 321) was used to cut the silicon wafers into 45 × 5 mm strips, which were cleaned individually by ultrasonication in de-ionized water to remove any particles that may have accumulated during dicing. The top adherend was coated with an Au/Pd thin film from one end of the strip to a length of 15 mm. The adhesion energy between the Au/Pd coating and the epoxy was fairly small ($\approx 0.07\,J/m^2$), which allowed an initial crack to form with minimal or no damage ahead of the crack front upon application of the load.

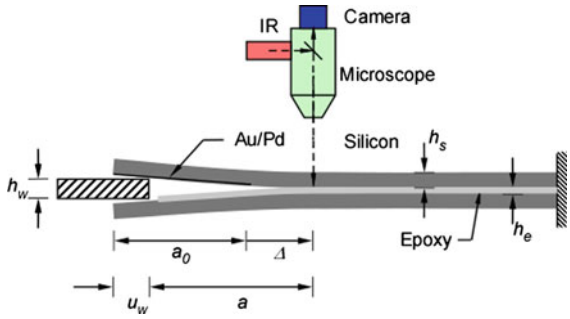

Fig. 1 Schematic of the DCB specimen and apparatus

The epoxy that was used in the experiments was prepared by mixing a resin (modified bisphenol-A epoxy, Araldite® GY502) and a hardener (polyamidoamine, Aradur®955) thoroughly in a 100:45 ratio by weight. This mixture was then degassed in a chamber to remove the bubbles in the epoxy. To prepare the specimen, a silicon strip was laid on a Teflon® tape with a 27 μm-thick shim at either end to control the thickness of the epoxy layer. A bead of the degassed epoxy was dropped on the silicon surface and spread out with a spatula. Then the silicon adherend with the partial Au/Pd coating was pressed on the bead with a weight to spread epoxy into a layer between the two silicon strips. The specimen was cured for 3 h at 65 °C and then allowed to cool slowly.

2.2 Infrared crack opening interferometry

In order to measure the NCOD, we exploited the transparency of silicon to infra-red and classical crack opening interferometry (Liechti 1993), which essentially uses the interference between the two rays reflected from the crack surfaces to determine the distance between them. The experiments were performed using an infrared microscope (Olympus BH2-UMA) that was fitted with an internal beam splitter and an IR filter (1,040 ± 15 nm) to provide the normal incident beam (Fig. 1). A digital camera (Lumenera Corporation, Infinity 3) with a resolution of 1,392×1,040 pixels captured the images (Fig. 2a). These were processed to determine the location of the crack front and the NCOD. For the normal incidence provided by the microscope, each transition from a dark to a bright fringe or *vice versa* indicates an increment in NCOD corresponding to a quarter of the IR wavelength ($\lambda = 260$ nm). Swadener and Liechti (1998) developed a method to determine the NCOD (δ) between fringes by measuring the light intensity I relative to the peak to peak intensity I_{pp} through:

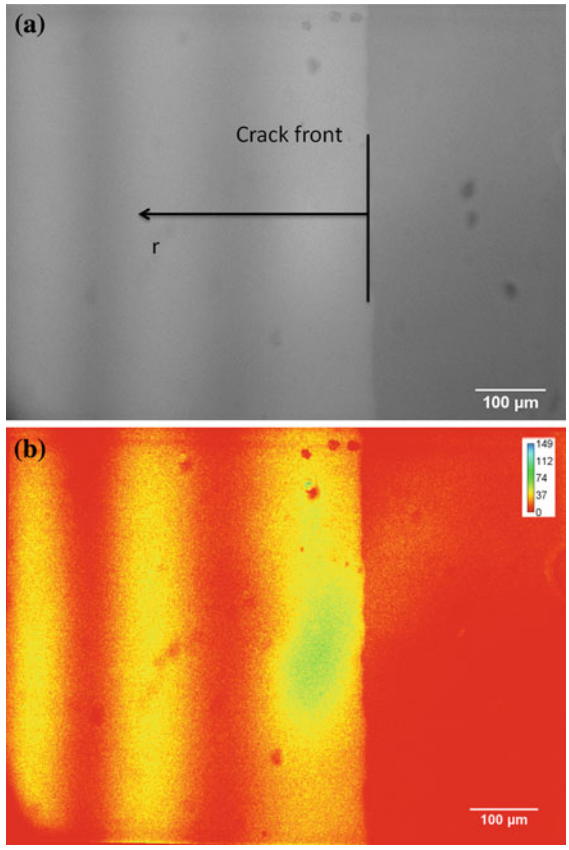

Fig. 2 A typical interferogram of the crack-front with the fringes due to crack opening and the dark area representing the bonded region of the silicon/epoxy interface. **a** A *grayscale image* and **b** a *red-green colored* image

$$\frac{I}{I_{pp}} = \frac{1}{2}\left[\pm 1 \mp \cos\left(\frac{4\pi\,|\delta|}{\lambda}\right)\right] \tag{1}$$

This improved the resolution by almost an order of magnitude, bringing it down to approximately 20 nm for the NCOD measurement.

A reference image was subtracted from every image in order to reduce the effect of the background signal. Figure 2b shows an example of the resulting image. Then, the intensity profiles along 15 adjacent pixel rows were extracted using the ImageJ (1.42q) software and averaged over these pixel rows in order to provide some smoothing of the raw data. This was then input to MATLAB® for curve fitting, typically using high order Gaussian curves that provided the best fit to the intensity profile plots (Fig. 3). The crack front was

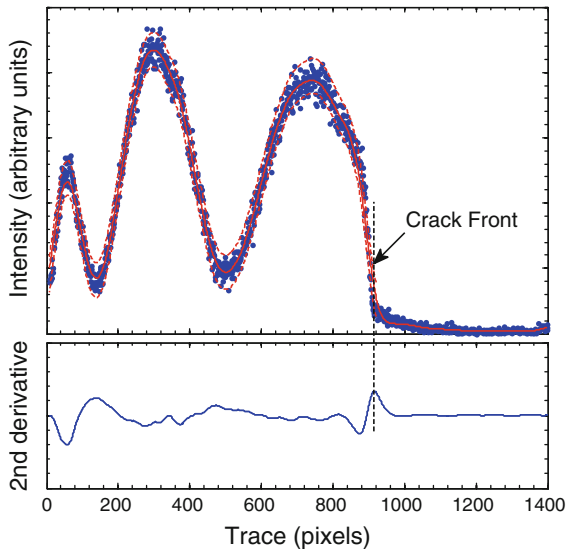

Fig. 3 An intensity profile and the curve fit to the data along with the 95th percentile bounds and the second derivative of the fit

identified by tracking the change in the slope of the intensity profile (i.e. the second derivative of the fit) and noting the location at which this change reached the first peak from the bonded region (dark area). This was also taken to be the location of the zero order fringe so that subsequent peaks and valleys corresponded to the locations of bright and dark fringes. The NCOD values were extracted between fringes using the fitted intensity values in Eq. (1). The average deviation of the data from the fit was used to arrive at the 20 nm uncertainty in the NCOD measurement.

2.3 Procedure

The experiment, a nominally mode-I DCB wedge test configuration, was conducted using a screw-driven wedge that could be inserted and removed under displacement control. The axial load was applied manually in 0.1 mm steps using a micrometer screw and was reacted at the un-cracked end of the specimen. The initial crack in the specimen was created when the 83.8 μm-thick wedge (h_w) was inserted into the specimen at the edge where the Au/Pd coating had been applied. The low adhesion between the Au/Pd film and the epoxy gave rise to immediate delamination at the interface upon insertion of the wedge. This initial delamination arrested precisely at the end of the Au/Pd film, beyond which the silicon/epoxy interface was undamaged. The Au/Pd coating thus provided good control over the initial crack length and the damage state of the interface.

Prior to crack growth, the wedge insertion was applied in 0.1 mm steps with a 120 s interval between them. At least one image of the crack front region was recorded at each step. As the onset of crack growth was anticipated, each loading step was maintained for 10 minutes while a time-lapse feature was used to allow interferograms to be taken at 5-s intervals in the crack-front region.

2.4 Measurements

The crack length a is defined as the distance between the wedge and the crack front (Fig. 1), which was determined by two measurements: the displacement of wedge insertion u_w and the distance Δ that the crack front advanced from the initial position. Thus,

$$a = a_0 + \Delta - u_w \tag{2}$$

where a_0 is the initial crack length. The fact that interference fringes remained visible throughout growth indicates that crack growth was predominantly interfacial in nature. This does not rule out the possibility of nanometer sized epoxy islands or ligament traces on the silicon side of the interface. Figure 4 shows the measured crack length with respect to the insertion displacement of the wedge. As can be seen, with the insertion of the wedge, the crack length decreased linearly to the point when the crack front began to advance and became nearly a constant as the crack growth reached a steady state. An interesting observation from the measurements is that the crack growth seems to exhibit a damped stick-slip behavior. The crack length first increased rapidly and arrested, and then the initial linear behavior resumed as the wedge was inserted further into the specimen until crack front advanced again. The increase in the crack length after the first 2-3 major advances reduced and eventually the crack growth did reach a steady state.

Figure 5 sketches the crack tip region and the cohesive zone, defining the coordinate systems used in the present study. The origin $x = 0$ is the location of the initial crack front, and $r = 0$ defines the moving crack front. The NCOD at the initial crack front ($x = 0$) is denoted δ^*. A cohesive zone ahead of the crack front

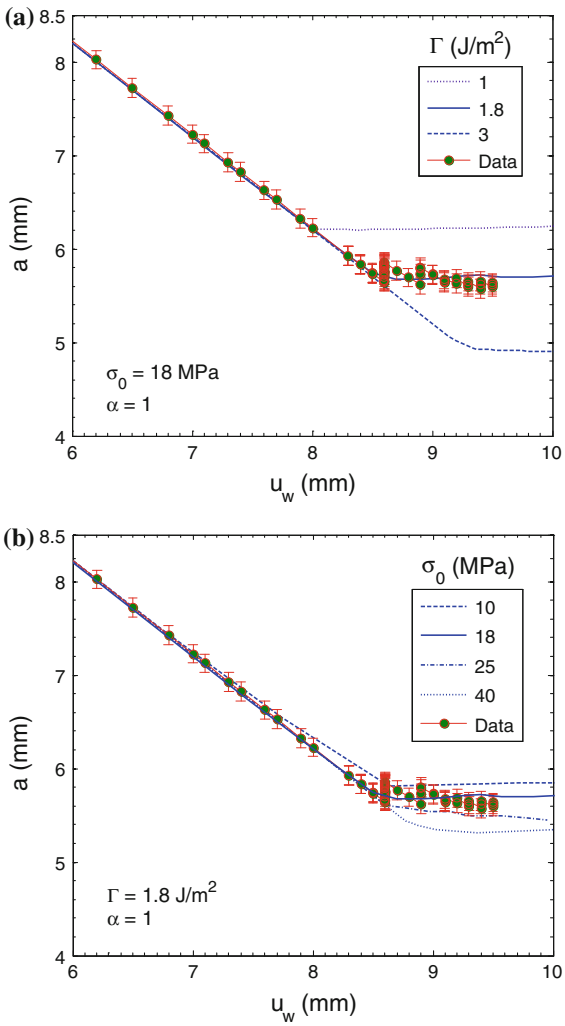

Fig. 4 Measurement of crack length with respect to wedge insertion, in comparison with numerical simulations with: **a** different interfacial toughness values and **b** different strength values

($x > 0$) is indicated by the interfacial tractions acting to close the opening of the interface. A typical set of NCOD profiles measured during crack opening and growth is displayed in Fig. 6. As can be observed, the crack front first remained stationary as the crack opened. Once the crack front began to move forward, the NCOD profiles seemed to retain their shapes, an indication of steady state. Interestingly, the NCOD profiles exhibit a knee-shaped kink close to the crack front. As will be discussed later, the significance of the kink is partly attributed to the presence of the epoxy layer in the DCB specimen.

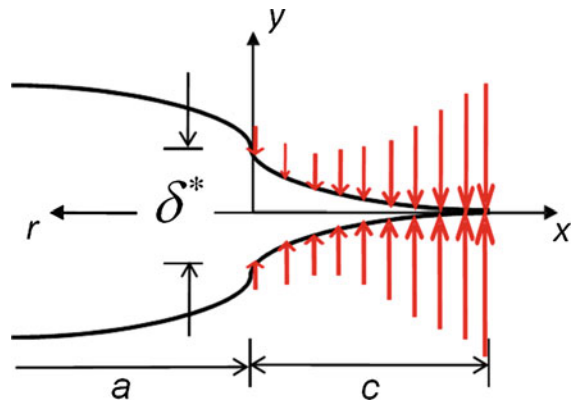

Fig. 5 A schematic of the crack front geometry and cohesive zone

3 Modeling and simulations

Two modeling approaches were taken to understand the interfacial crack growth in the DCB wedge tests. The first was an analytical approach by combining a cohesive zone model with simple beam theory. The second was a numerical model using the finite element method in ABAQUS® that accounted for the two silicon strips, the epoxy layer, and the adhesive interactions across the silicon/epoxy interface.

3.1 Cohesive zone models

The approach of cohesive zone modeling is particularly suitable for adhesion and debonding of interfaces between dissimilar materials (Hutchinson and Evans 2000). Typically, a nonlinear traction-separation relation is used to simulate crack opening and growth at an interface. Previous studies (Tvergaard and Hutchinson 1992; Feraren and Jensen 2004; Li et al. 2005; Parmigiani and Thouless 2007) have suggested that the strength and toughness are the two most important parameters, and that the shape of the traction-separation relation is secondary. In the present study, two types of traction-separation relations were used, one with linear softening and the other with exponential softening, as illustrated in Fig. 7. Subject to an opening stress σ, the interface first opens elastically in both cases with the initial stiffness (K_0) until the stress reaches the strength of the interface ($\sigma = \sigma_0$), at which point damage initiation occurs. A damage parameter D is used to describe the state of the interface, which evolves from 0 to 1 based on a damage evolution rule:

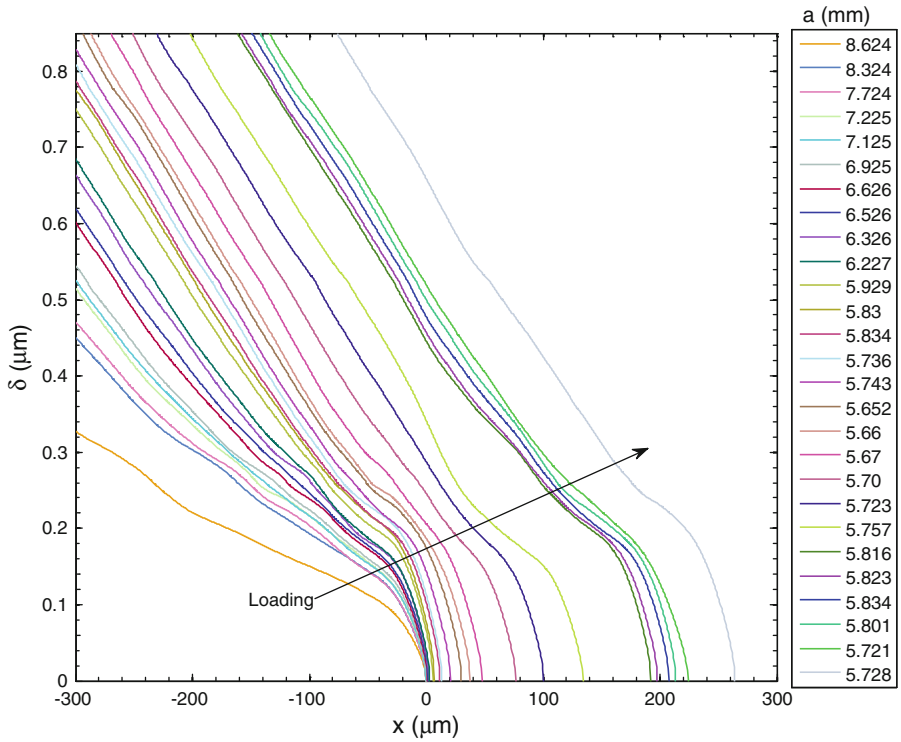

Fig. 6 The normal crack opening displacement (NCOD) measured by IR-COI as a function of the distance from the initial crack front ($x = 0$)

$$D = \frac{\delta_c\,(\delta_m - \delta_0)}{\delta_m\,(\delta_c - \delta_0)} \tag{3}$$

for the linear softening and

$$D = 1 - \frac{\delta_0}{\delta_m}\left[1 - \frac{1 - \exp\left(-\alpha\frac{\delta_m - \delta_0}{\delta_c - \delta_0}\right)}{1 - \exp\left(-\alpha\right)}\right] \tag{4}$$

for the exponential softening. Here, $\delta_0 = \sigma_0/K_0$ is the critical separation for damage initiation, δ_c is the critical separation for fracture, and δ_m is the maximum separation experienced by the interface element over the entire loading history. The parameter α controls the shape of the exponential softening.

Once $\delta_m > \delta_0$, the damage parameter D increases as the opening displacement increases ($0 < D < 1$), and the opening stress is related to the opening displacement as

$$\sigma = (1 - D)\,K_0\delta_m \tag{5}$$

For the case with the linear softening, when $\delta_0 \le \delta_m \le \delta_c$, the stress decreases linearly:

$$\sigma = \sigma_0\frac{\delta_c - \delta_m}{\delta_c - \delta_0} \tag{6}$$

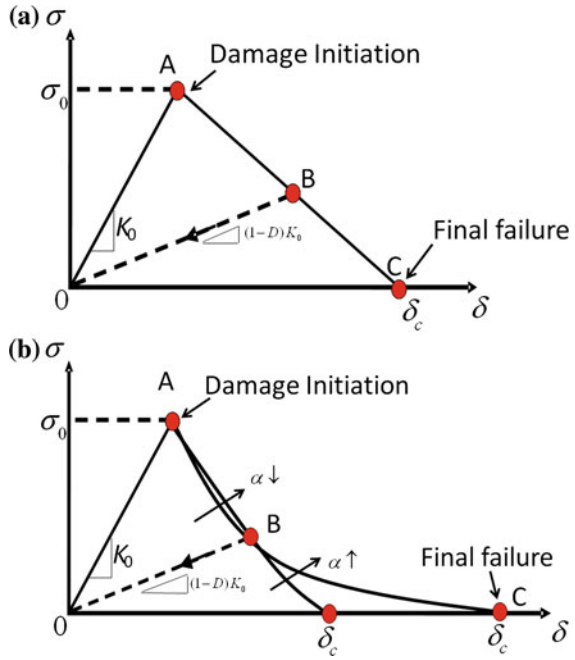

Fig. 7 Two types of traction-separation relation: **a** a bilinear model, and **b** a linearly elastic relation followed by exponential softening. The quantity δ_m in Eqs. (3)–(7) equals δ during loading (crack opening) but remains a constant during unloading (crack closing)

For the exponential softening, this portion of the traction-separation relation follows

$$\sigma = \sigma_0 \left(1 - \frac{1 - \exp\left(-\alpha\left(\frac{\delta_m - \delta_0}{\delta_c - \delta_0}\right)\right)}{1 - \exp(-\alpha)}\right) \tag{7}$$

In both cases, when $\delta_m = \delta_c$, $D = 1$ and $\sigma = 0$ indicating that the interface element is fully fractured. During any unloading prior to fracture, the damage parameter remains constant (irrecoverable) and the stress decreases linearly as the opening displacement decreases, with the slope $K = (1 - D) K_0$, as illustrated in Fig. 7. Any subsequent reloading follows this slope until the softening part of the traction-separation relation is again encountered.

For each traction-separation relation, the fracture toughness is obtained as

$$\Gamma = \int_0^{\delta_c} \sigma(\delta) d\delta \tag{8}$$

For the linear softening model, $\Gamma = \frac{1}{2}\sigma_0\delta_c$. For the exponential softening, $\Gamma = \frac{1}{2}\sigma_0\delta_c\gamma\left(\frac{\delta_0}{\delta_c}, \alpha\right)$, with $\gamma(x, \alpha) = x + 2(1 - x)\frac{e^\alpha - 1 - \alpha}{\alpha(e^\alpha - 1)}$.

To account for the effects of mode mix, the traction-separation relations can be defined separately for the opening and shearing modes (modes I, II, and III), each with a set of similar parameters as the opening mode. In general, both the criteria for damage initiation and final fracture depend on mode mix (Mei et al. 2010). In the present study, the effect of mode mix is ignored, considering predominantly mode I fracture in the DCB specimen.

3.2 Analytical approaches

From simple beam theory, the energy release rate (or J-integral) for the crack growth in a symmetric DCB specimen (Fig. 8a) is

$$J = \frac{12P^2a^2}{Eh^3b^2} = \frac{3Eh^3d^2}{16a^4} \tag{9}$$

where P is the applied force, d is the crack opening at the loading point, E is the Young's modulus of the beam, h is the thickness, and b is the width. Eq. (9) is obtained under several assumptions: (1) the effect of transverse shear is negligible; (2) rotation of the beam section at the crack tip (i.e., root rotation) is negligible;

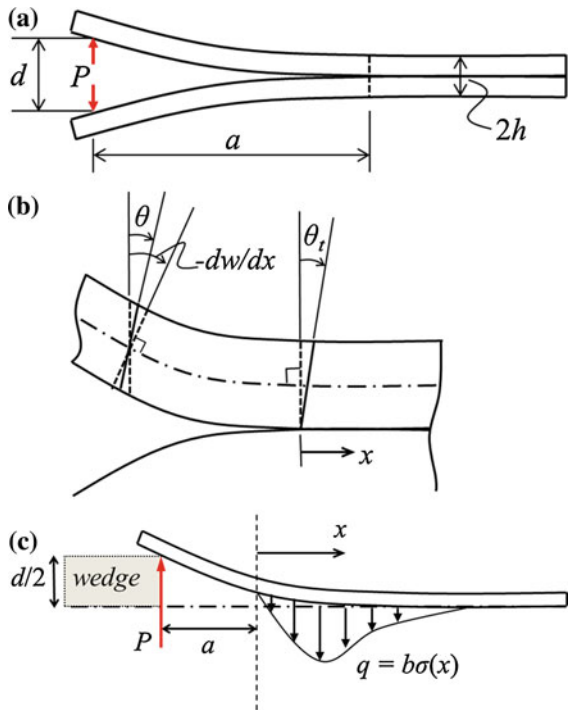

Fig. 8 Schematics of DCB models. **a** A simple beam model with zero root rotation; **b** part of a Timoshenko beam model near the crack tip with an angle of root rotation; **c** the upper beam in a wedge-loaded DCB specimen with cohesive interactions ahead of the crack tip

(3) the size of the cohesive zone ahead of the crack tip is negligibly small. These assumptions are typically justified when $a \gg h$.

A large number of authors have suggested corrections to Eq. (9) (Gillis and Gilman 1964; Wiederhorn et al. 1968; Kanninen 1973; Chow et al. 1979; Fichter 1983; Williams 1989; Williams and Hadavinia 2002; Li et al. 2004). By including the effect of transverse shear, Li et al. (2004) obtained

$$J = \frac{12P^2a^2}{Eh^3b^2}\left(1 + 0.674\frac{h}{a}\right)^2 \tag{10}$$

which is in close agreement with the result obtained by using the Timoshenko beam theory (Gillis and Gilman 1964; Wiederhorn et al. 1968). The effect of root rotation was discussed by Li et al. (2004), who concluded that root rotation should not be considered as an independent contributor to the energy release rate. Root rotation may occur as a result of the shear effect and the elastic deformation ahead of the crack tip. "Appendix A" presents a DCB analysis with the shear effect and root rotation (Fig. 8b), which leads to a formula

for the energy release rate in terms of the opening displacement:

$$J = \frac{3Eh^3d^2}{16a^4}\left(1 - 2.691\frac{h}{a} + 4.485\frac{h^2}{a^2}\right) \quad (11)$$

Moreover, the effect of the cohesive zone was found to be significant when the interfacial properties satisfy the condition, $\frac{E\Gamma}{\sigma_0^2 h} > 0.4$, in the regime of large-scale bridging (Bao and Suo 1992; Li et al. 2004). In particular, elastic foundation models have been used to analyze the effect of elastic interactions across the interface (Kanninen 1973; Chow et al. 1979; Williams 1989; Williams and Hadavinia 2002). Here we extended the elastic foundation model to include the softening part of the traction-separation relation as an augmented analytical approach for the DCB specimen (Fig. 8c). The details are presented in "Appendix B", with the key results summarized as follows.

Start with an initial crack in the DCB specimen, where the interface ahead of the crack tip is undamaged ($D = 0$). As the crack opens up, the interface opens elastically until the crack tip opening displacement (CTOD, δ^*) reaches the critical value (δ_0) for damage initiation. When $\delta^* < \delta_0$, the interface ahead of the crack tip behaves like an elastic foundation, and the energy release rate is obtained as

$$J = \frac{12P^2a^2}{Eb^2h^3}\left(1 + \xi\frac{h}{a}\right)^2 \quad (12)$$

where $\xi = \left(\frac{E}{6K_0h}\right)^{\frac{1}{4}}$. Incidentally, Eq. (12) is similar to Eq. (10) in spite of the different physical models. In terms of the loading displacement, the energy release rate is

$$J = \frac{3Eh^3d^2}{16a^4}\left(\frac{1 + \xi\frac{h}{a}}{1 + 3\xi\frac{h}{a} + 3\xi^2\frac{h^2}{a^2} + 1.5\xi^3\frac{h^3}{a^3}}\right)^2 \quad (13)$$

when $\xi \ll \frac{a}{h}$, Eqs. (12) and (13) recover the simple solution in Eq. (9).

When $\delta^* > \delta_0$, a damage zone of length c develops ahead of the crack tip. Within the damage zone ($0 < x < c$), the damage parameter D varies between 0 and 1 and the interface is in the softening phase. Ahead of the damage zone $x > c$, the interface is undamaged ($D = 0$) and elastic interactions are active. For a given traction-separation relation, we solve the beam equation in different parts and determine the damage zone size as well as the CTOD. The energy release rate is then calculated by the J-integral over a contour around the crack tip and enclosing the entire cohesive zone (both damaged and undamaged parts). The result however depends on the traction-separation relation. For the bilinear model (Fig. 7a), we obtain that

$$J = \frac{2\Gamma\left(\delta^* - \delta_0\right)}{\delta_c - \delta_0} - \frac{\sigma_0\left(\delta^{*2} - \delta_0^2\right)}{2(\delta_c - \delta_0)} + \frac{1}{2}\sigma_0\delta_0 \quad (14)$$

where δ^* is obtained implicitly as a function of the crack length a and the opening d. For the DCB specimen in the wedge test (Fig. 1), $d = h_w$ and δ^* is a function of a (see "Appendix B", Fig. A3). The analytical solution is only valid when $\delta^* \leq \delta_c$. When δ^* reaches δ_c, $J = \Gamma$ and the crack front advances. Subsequently, the crack grows under steady state conditions with a constant crack length ($a = a_{ss}$) and a constant damage zone size ($c = c_{SS}$).

The calculation of the J-integral is critical for determination of the interfacial traction-separation relation. In the analytical approaches being considered here, the J-integral depends on the interfacial properties and cannot be determined precisely without knowing the traction-separation relation *a priori*. Figure 9 plots the J-integral for the wedge-loaded DCB specimen as a function of the crack length, comparing the three different formulae with the numerical results from finite element models. Using Eq. (13), the interaction across the interface is purely elastic, which predicts an energy release rate slightly lower than Eq. (9). Using Eq. (14), the interfacial interaction includes a damage zone. However, the predicted J-integral is nearly identical to Eq. (13), except for the prediction of steady-state crack growth when $J = \Gamma$. Therefore, Eq. (13) may be used

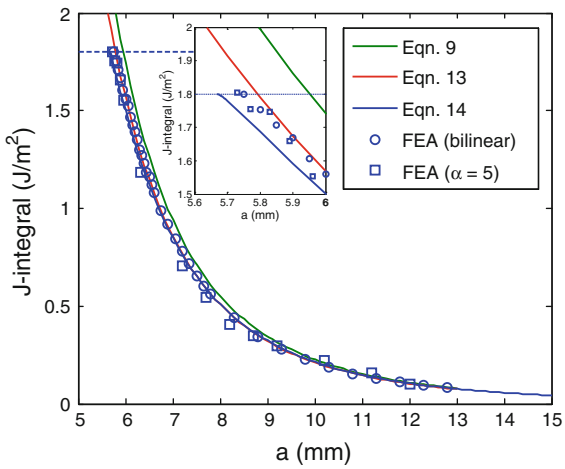

Fig. 9 J-integral as a function of the crack length, comparing the results from different models. The *inset* shows the close-up view near the fracture toughness $\Gamma = 1.8$ J/m^2

as an approximation for the J-integral, which agrees more closely with the finite element simulations than Eq. (9). Moreover, Eq. (11) is very close to Eq. (13), but without the need to assume a stiffness for the elastic interaction.

3.3 Finite element simulations

To simulate interfacial delamination of the wedge-loaded DCB specimen, we developed a two-dimensional, tri-layer finite element model in ABAQUS, with a layer of cohesive elements (COH2D4) for the interface between the top silicon beam and the epoxy layer. Both silicon beams and the epoxy layer were modeled by plane-strain quadrilateral elements (CPE8R), with linear elastic properties (Young's modulus: $E_{Si} = 170$ GPa and $E_e = 2.03$ GPa; Poisson's ratio: $\nu_{Si} = 0.22$ and $\nu_e = 0.36$). The wedge was modeled as a rigid body with frictionless, hard contact with the surface of each silicon beam. The traction-separation relation with either linear or exponential softening was used for the cohesive elements. As was shown in Fig. 7, the following parameters are required to define the bilinear traction-separation relation: the initial elastic stiffness K_0, the interfacial strength σ_0, and the interface toughness Γ. For the exponential softening, a shape parameter α is required in addition to the other three

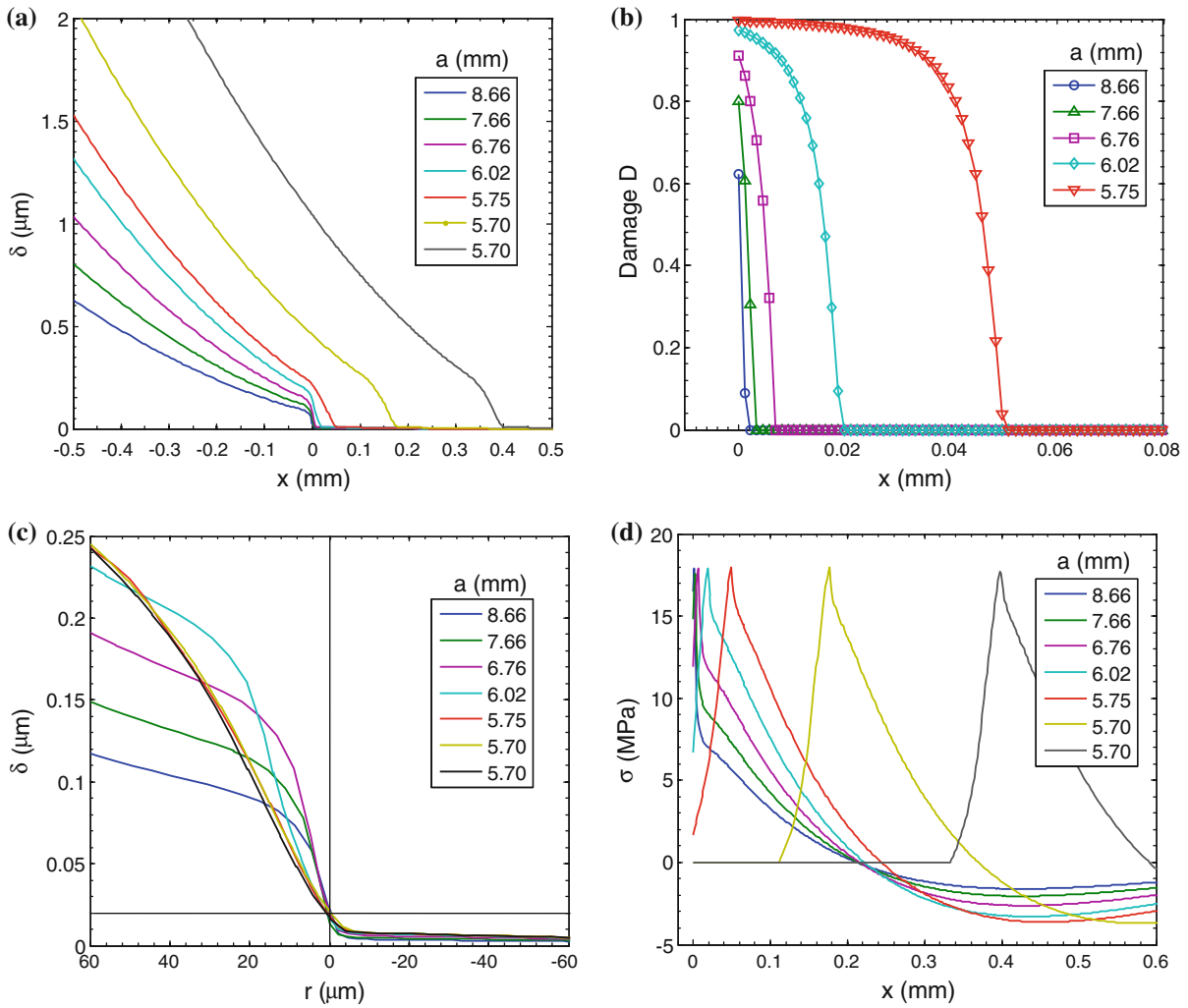

Fig. 10 Numerical results from a finite element simulation with the cohesive interface model ($\Gamma = 1.8$ J/m^2, $\sigma_0 = 18$ MPa, and $\alpha = 1$): **a** NCOD, **b** damage evolution, **c** NCOD near the crack tip, and **d** normal traction along the interface

parameters. It was found that the initial stiffness (K_0) plays a secondary role compared to the other parameters. In the present study, we fixed the interface stiffness as $K_0 = 2 \times 10^{15}$ N/m^3, but varied the strength, toughness and α to compare with the experiments.

The simulation was conducted in two steps. First, the silicon beams were given an opening displacement at the fractured end to the point that the wedge could be inserted. Next, with the wedge in between, the beams were further separated by displacing the wedge in the x-direction (Fig. 1). Figure 10 shows the numerical results from a finite element simulation using the traction-separation relation with $\Gamma = 1.8$ J/m^2, $\sigma_0 = 18$ MPa, and $\alpha = 1$ for exponential softening. In Fig. 10a, the NCOD is plotted as a function of x with $x = 0$ at the initial crack tip. As the wedge was inserted toward the crack tip, the crack opened up and a cohesive zone developed ahead of the initial crack tip. In the finite element model, the location of the crack tip can be identified by the damage parameter D, which equals 1 to the left of the crack tip but is less than 1 to the right of the crack tip. As shown in Fig. 10b, for each interface element ($x > 0$), D increased from 0 to 1 and crack growth started when the damage parameter of the first interface element reached 1. However, in an experiment, it may not be possible to precisely determine the location of the crack tip since the damage cannot be measured directly. On the other hand, the minimum NCOD that could be measured by the IR-COI technique is about 20 nm. Thus we defined the *experimental* crack tip at the location with $\delta_n = 20$ nm. The crack lengths (a) in Fig. 10 were then calculated by Eq. (2) with Δ being the distance between the experimental crack tip and the initial crack tip. In Fig. 10c, the NCOD is plotted as a function of r, with $r = 0$ at the location of the experimental crack tip that moved as the crack grew. The scale has been magnified in Fig. 10c in order to bring out the development of the cohesive zone near the crack tip. The horizontal line corresponds to $\delta = 20$ nm that was used to determine the location of the crack tip. By this definition, crack growth started at a crack length of approximately 6.02 mm and reached a steady state at 5.70 mm. The NCOD profiles converged onto the steady state as expected. We note that the critical separation ($\delta_c = 237.5$ nm) for the traction-separation relation used in this simulation is much larger than 20 nm. Consequently, normal traction is expected to act along part of the crack surfaces ($r > 0$), which would decrease the crack opening compared to the traction-free crack surfaces. Prior to the steady state growth, the cohesive zone was not fully developed, and thus the NCOD close to the crack tip were larger than the steady state NCOD. The order was reversed further away from the crack tip.

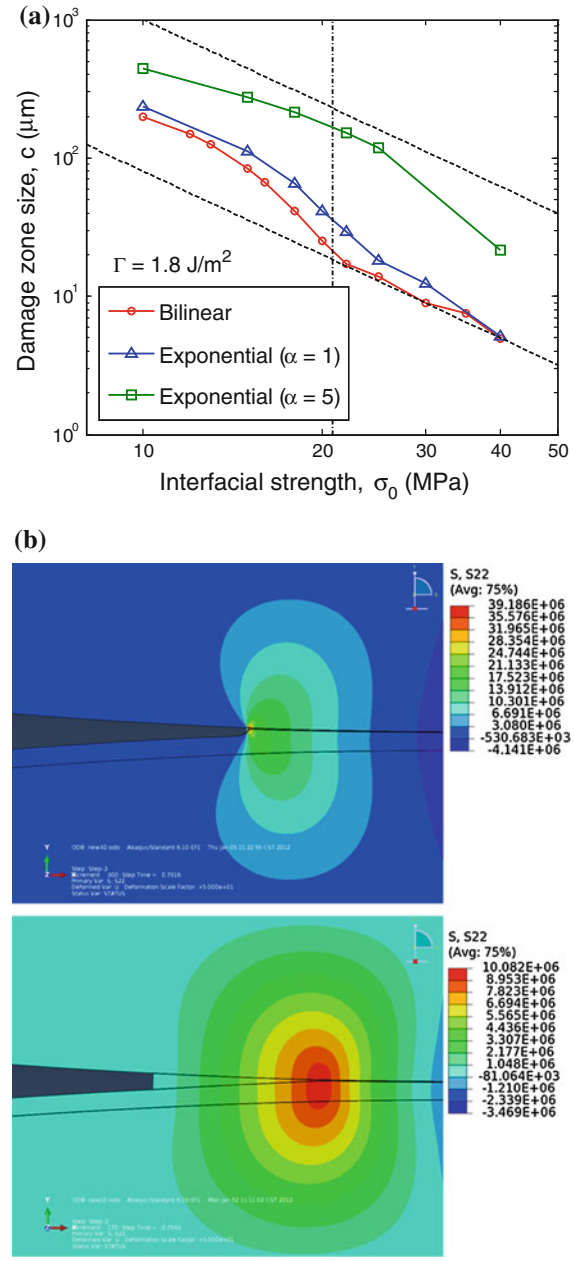

Fig. 11 **a** Steady-state damage zone size as a function of interfacial strength. **b** Stress distribution near the crack tip for small-scale bridging ($\sigma_0 = 40$ MPa and $c = 21.7\,\mu$m) and large-scale bridging ($\sigma_0 = 10$ MPa and $c = 439.2\,\mu$m)

The distribution of the normal traction along the interface ahead of the initial crack tip is shown in Fig. 10d. The traction was tensile within the damage zone ($0 < D < 1$). Beyond the damage zone, the interaction across the interface was elastic with a transition from tensile to compressive, which is characteristic of the elastic foundation behavior. The peak traction corresponded to the interfacial strength ($\sigma_0 = 18$ MPa). To its right, the traction was lower because it had not reached the strength (thus no damage). To its left, the traction was lower because the interface had been damaged and thus was softening.

The cohesive zone in the present model consisted of a damage zone and an elastic zone. The size of the elastic zone, which depends on the interfacial stiffness K_0, is typically much larger than the damage zone. The size of damage zone on the other hand depends on the interfacial strength and toughness. Figure 11a shows the steady-state damage zone size as a function of the interfacial strength for a constant toughness ($\Gamma = 1.8$ J/m^2). In general, the steady-state damage zone size decreases as the interfacial strength increases, following roughly the scaling $c \sim \sigma_0^{-2}$ as indicated by the two parallel lines. Moreover, it is found that the damage zone size depends on the shape of the traction-separation relation, with a larger damage zone for exponential softening than for linear softening, although the dependence is relatively weak. In all cases, the damage zone size became insensitive to the strength for relatively high strength values, where the condition of small-scale bridging prevails. The vertical line in Fig. 11a indicates the condition $\frac{E\Gamma}{\sigma_0^2 h} = 0.4$ as suggested by Li et al. (2004). To its left, $\frac{E\Gamma}{\sigma_0^2 h} > 0.4$, large-scale bridging occurs and the damage zone size increases sharply with decreasing strength. Figure 11b shows two examples by the finite element simulations, for small-scale and large-scale bridging, respectively.

4 Results and discussion

As indicated in the Introduction, two methods can be used to extract the traction-separation relations: the direct and iterative methods. The former relies on differentiating the J-integral with respect to the measured NCOD at the initial crack tip, while the latter involves comparison of the numerical simulations with the measurements to determine the key parameters of the traction-separation relation. The results from both methods are presented and compared in this section.

4.1 Direct method

The direct method considered here relied on calculating the J-integral with the measured crack length and taking its derivative with respect to the measured NCOD at the initial crack tip (Sørensen and Jacobsen 2003; Sørensen and Kirkegaard 2006; Högberg et al. 2007; Zhu et al. 2009). Alternatively, with simultaneous measurements of the force and opening displacement at the loading point along with the NCOD at the crack tip, it is possible to determine the traction-separation relation experimentally without using the analytical model (Stigh and Andersson 2000). In the present work, the force by wedge loading was not measured, and we calculated the J-integral based on the analytical approaches in Sect. 3.2, namely

$$J = \frac{3E_{Si}\,(h_w - h_e)^2\,h_s^3}{16a^4}\psi\left(\frac{a}{h_s}\right) \tag{15}$$

where h_w, h_e and h_s are the thicknesses of the wedge, epoxy layer and silicon strip, respectively. The dimensionless function ψ may take different forms depending on the analytical model. Here we take Eq. (13) based on the elastic foundation model, which is a better approximation than Eq. (9) in comparison with finite element simulations (Fig. 9). The Young's modulus of the silicon ($E_{Si} = 170$ GPa) (Brantley 1973) was determined in a separate three point bending test. At each loading step, the J-integral was calculated using the measured crack length (Fig. 4) and linked with the measured NCOD (Fig. 6). In particular, the NCOD at the initial crack tip ($x = 0$) was denoted as δ^* (Fig. 5). As a result, the J-integral was obtained as a function of δ^* shown in Fig. 12. For comparison, the J-integral obtained by Eq. (9) is also plotted along with two analytical results for the bilinear and exponential softening models. The parameters for the analytical models were determined from the iterative method in Sect. 4.2.

Within the resolution of the NCOD measurements by IR-COI, there was an initial rise in the value of the J-integral up to 0.66 J/m^2 before δ^* became measureable. The increase in J-integral thereafter was still quite steep and reached the maximum of 1.88 J/m^2 before it was stabilized. As shown in Fig. 4, the crack front advanced in a stick-slip fashion, leading to the J-integral values oscillating at or below 1.88 J/m^2, which

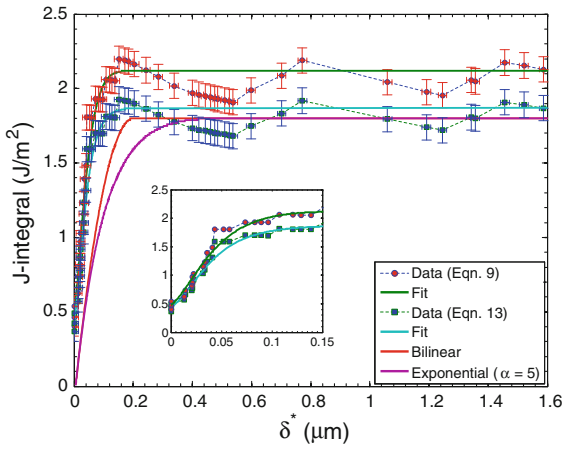

Fig. 12 J-integral as a function of the opening displacement at the initial crack tip

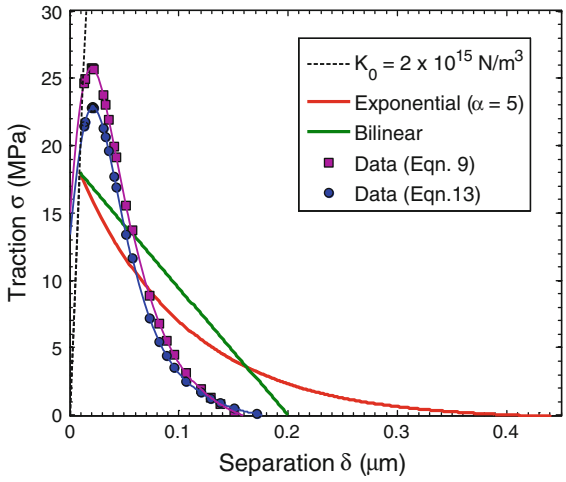

Fig. 13 Traction-separation relations obtained from the direct method, in comparison with the bilinear and exponential softening models used in the iterative method

was deemed the toughness of the silicon/epoxy interface. A polynomial function was used to fit the rising portion of the data in Fig. 12 followed by the constant value ($\Gamma = 1.88$ J/m^2) for the steady state, disregarding the oscillation due to stick-slip.

As shown in Fig. 5, with a cohesive zone and δ^* as the opening at the initial crack tip, a contour integral enclosing the cohesive zone gives the J-integral as

$$J = \int_0^{\delta^*} \sigma(\delta) d\delta, \tag{16}$$

where the traction $\sigma(\delta)$ acts across the interface over the cohesive zone. By the path independence of the J-integral, it can also be calculated from Eq. (15). Consequently, the traction-separation relation under mode I conditions can be determined by taking the derivative of the J-integral with respect to δ^* (Sørensen and Jacobsen 2003; Sørensen and Kirkegaard 2006)

$$\sigma(\delta^*) = \frac{dJ}{d\delta^*}. \tag{17}$$

Note that although this is a mode I dominant case, the elastic mismatch across the silicon/epoxy interface does give rise to small tangential component for the crack opening displacements. Nonetheless, since the normal crack opening displacements were the only ones measured with IR-COI, only the normal tractions were determined by Eq. (17). In the present study, we have not pursued the measurement of the tangential displacements for the general mixed-mode traction-separation relation.

The derivative of the polynomial fit to the data in Fig. 12 was taken, thereby obtaining the traction-separation relation for the silicon/epoxy interface (Fig. 13). The traction-separation relations with linear and exponential softening used in the finite element simulations are plotted alongside. The traction-separation relation obtained via the direct method rises steeply to a strength of 22 MPa. The softening that follows is relatively sharp and terminated at the critical value of the NCOD, $\delta_c \sim 0.18\,\mu$m. The area underneath the curve gives the interface toughness, $\Gamma = 1.88$ J/m^2. These values give rise to the dimensionless parameter $\frac{E_{Si}\Gamma}{h_s\sigma_0^2} = 2.35$, which places it in the large-scale bridging regime (Li et al. 2004).

4.2 Iterative method

The iterative method assumes a particular form of the traction-separation relation with the key parameters determined by comparing numerical simulations with experimental measurements. For the bilinear traction-separation relation (Fig. 7a), three parameters are to be determined; the toughness Γ, the strength σ_0, and the stiffness K_0. For exponential softening (Fig. 7b), an additional parameter α is needed. For the present study, we took $K_0 = 2 \times 10^{15}$ N/m^3 and determined the other three parameters in three steps to obtain a traction-separation relation that resulted in NCOD that were in good agreement with the measured val-

ues near the crack tip. In short, the toughness was first determined by comparing the steady-state crack length of the finite element model with the experiment, considering that the other two parameters have less effect on the crack length. Next, the interfacial strength was varied to compare the steady-state NCOD from the numerical simulations with the measurements, and the strength value that yielded the best fit was taken in the second step. Finally, the exponential softening with a particular shape parameter was used to bring the NCOD into better agreement than the linear softening.

As shown in Fig. 4, the steady-state crack length obtained from the numerical simulations depends sensitively on the interface toughness. As the first step, a toughness of 1.8 J/m^2 was determined to provide the best agreement with the measured steady-state crack length. The same toughness was obtained for both the bilinear and exponential softening. On the other hand, it was found that the dependence of the steady-state crack length on the interfacial strength was much weaker (Fig. 4b).

Figure 14 shows the effect of the interfacial strength on the NCOD during steady state growth using the traction-separation relation with the interface toughness $\Gamma = 1.8$ J/m^2 and $\alpha = 5$ for exponential softening. With $r = 0$ defining the location of the moving crack tip, we compared the numerical results with the measurements and found that the strength of 18 MPa provided the best agreement. As noted in Fig. 6, a knee was present in the measured NCOD. Similar features are also apparent in the numerical results for relatively large strengths ($\sigma_0 > 15$ MPa) in Fig. 14. This knee may be attributed to two factors: the presence of the epoxy layer and the interfacial strength. When numerical simulations were conducted with a bilayer model without the epoxy (Mei 2011), the knee was absent. The epoxy layer is relatively soft with moderately large deformation near the crack tip as illustrated in Fig. 11b. In addition, the knee disappeared as the interfacial strength was low (e.g. $\sigma_0 = 10$ MPa). In this case, the large–scale bridging reduced the stress intensity at the crack tip, resulting in a nearly linear NCOD profile.

It was found that the steady-state NCOD near the crack tip depended slightly on the shape of the traction-separation relation. The comparison is made (Fig. 15) using the linear softening and exponential softening with different values of α, with the fixed values for the toughness and strength. For $\alpha \leq 5$ there was

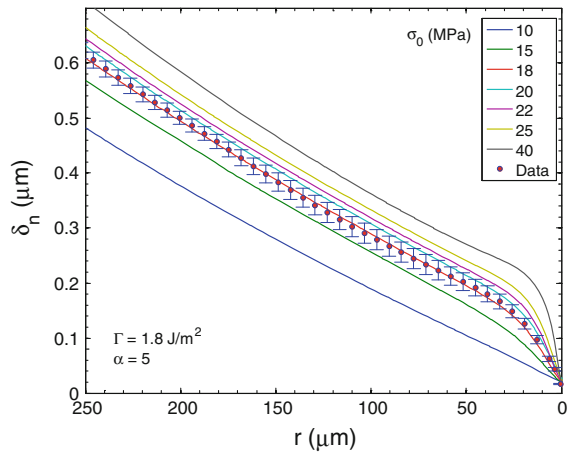

Fig. 14 Effect of interfacial strength on steady state NCOD, in comparison with the experimental data. The value of σ_0 that provided best fit to the data was 18 MPa

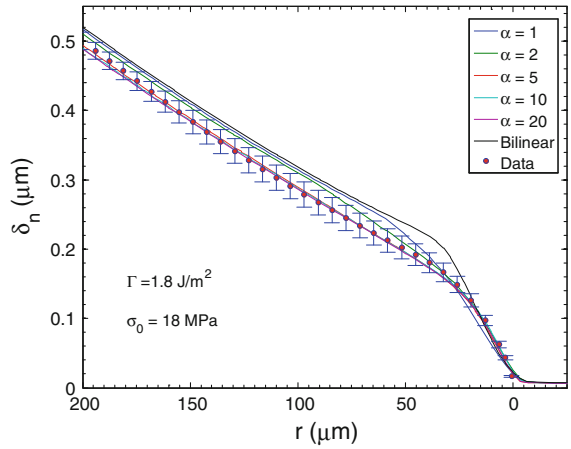

Fig. 15 Effect of the shape parameter α on steady state NCOD, in comparison with the experimental data. The values of α that provided best fit to the data were 5 and above

a noticeable difference in the numerical results for the NCOD, but the results converged for $\alpha > 5$. In comparison with the measured NCOD, $\alpha = 5$ was chosen for the best fit. On the other hand, without the shape parameter, the bilinear traction-separation relation cannot achieve the same level of agreement. Consequently, this iterative method yielded a traction-separation relation for the silicon/epoxy interface with $\Gamma = 1.8$ J/m^2, $\sigma_0 = 18$ MPa and $\alpha = 5$.

To summarize, the parameters for the traction-separation relation of the silicon/epoxy interface are listed in Table 1. The toughness and the strength obtained via the direct method were respectively 4.4

Table 1 Key parameters for the traction-separation relation of a silicon/epoxy interface extracted from the direct and iterative methods

Method	Γ (J/m^2)	σ_0 (MPa)	δ_c (nm)
Direct	1.88	22.0	176
Iterative (bilinear)	1.8	18.0	200
Iterative (exponential)	1.8	18.0	450

and 22 % higher than the values obtained by the iterative method. The difference in the toughness values is attributed to the use of the approximate solution for the J-integral in the direct method. As elaborated in Fig. 9, the analytical solution typically overestimates the J-integral compared to the finite element model. The difference decreases as the crack length increases and diminishes for long cracks. The discrepancy in the obtained strength values is larger, partly due to the fact that the strength by the direct method was obtained by differentiating the overestimated J-integral with respect to the opening displacement δ^*. Therefore, it is concluded that the accuracy of the direct method relies on the calculation of the J-integral, which may be improved by using the augmented analytical models as discussed in Sect. 3.2.

The interfacial properties of this epoxy have been studied previously when bonded to glass (Swadener and Liechti 1998; Swadener et al. 1999) and sapphire (Mello and Liechti 2006). The mode-I toughness levels of the epoxy when bonded with glass and sapphire were 1.8 J/m^2 and 1.5 J/m^2, respectively, similar to the toughness measured here. The interfacial strength however shows a stark difference compared to the cases using glass and sapphire adherends. First, we note that the strengths (Table 1) obtained for this silicon/epoxy interface are significantly less than the plateau stress of the epoxy, which was estimated using bulk material properties by Swadener et al. (1999) to be 60 MPa. The glass/epoxy interface (Swadener and Liechti 1998; Swadener et al. 1999) displayed a strength value of approximately 94 MPa, which is about 1.5 times the plateau stress of the epoxy, whereas the sapphire/epoxy interface (Mello and Liechti 2006) had a higher value of approximately 120 MPa. As a result, the critical NCODs obtained here for the silicon/epoxy interface (Table 1) are much larger than the corresponding values for the glass/epoxy and sapphire/epoxy interfaces, which were 35 and 28 nm, respectively. The reasons for the differences in the strength and critical opening displacement are beyond the scope of this paper but may be brought out subsequently in fractographic and spectroscopic analyses (Swadener et al. 1999; Mello and Liechti 2006). Furthermore, because the interfacial strength of the silicon/epoxy interface was much lower than the plateau strength of the epoxy, we do not expect the toughness of this interface to display much mode-mix dependence. This expectation has yet to be borne out by mixed-mode experiments. Both the interfacial traction-separation relations obtained for the glass/epoxy and the sapphire/epoxy interfaces were bilinear in form, which was not the case for the directly determined traction-separation relation here. Furthermore, the best result from the iterative approach was exponential in form.

5 Conclusions

Crack opening interferometry provided valuable insights into the direct and iterative methods of extracting interfacial traction-separation relations. The mode-I traction-separation relation of an epoxy/silicon interface was first extracted via the direct method by making use of interferometric measurements of the local crack opening displacements in a wedge test along with an analytical solution of the J-integral. As an example of the iterative approach, we compared measured values of crack length and crack opening displacements with numerical solutions obtained from a series of candidate traction-separation relations. A three-step procedure was used to determine the three key parameters for the traction-separation relation that resulted in close agreement with the interferometric measurements. The traction-separation relations extracted by the two methods compared reasonably well. The direct method yielded the most accurate results when the J-integral was calculated based on a beam on elastic foundation model. In exploring the iterative method, which made use of finite element simulations that incorporated the candidate traction-separation relations with linear and exponential softening, it was found that the shape of the traction-separation relation, in addition to the interfacial toughness and strength, was needed to bring solutions for NCOD into optimal registration with measured values. On the other hand, the direct method retained its prom-

ise of ease of parameter extraction with little cost in accuracy.

Acknowledgments The authors gratefully acknowledge funding of this work by Semiconductor Research Corporation.

Appendix A: DCB analysis with shear effect and root rotation

The static Timoshenko beam theory (Fig. 8b) takes into account the shear effect so that the angle of rotation of each cross section of the beam consists of two parts:

$$\theta = -\frac{dw}{dx} - \frac{V}{\kappa \mu A} \tag{A.1}$$

where w is the deflection, V is the shear force, μ is the shear modulus, A is the area of the cross-section, and κ is the shear coefficient. The shear coefficient depends on the shape of the cross section. For a rectangular cross section, $\kappa = 0.833$ (Graff 1975).

The governing equation for the deflection is

$$\frac{d^2w}{dx^2} = \frac{M}{EI} - \frac{1}{k\mu A}\frac{dV}{dx} \tag{A.2}$$

where M is the bending moment, E is the Young's modulus, and $I = bh^3/12$ for a beam of thickness h and width b.

For a DCB specimen, consider the top beam only, with $x = 0$ at the crack tip (Fig. 8b). The shear force is a constant between the loading point and the crack tip ($-a < x < 0$): $V = P$ and $M = P(x+a)$. The boundary conditions at the crack tip are: (1) $w(x = 0) = 0$; (2) $\theta(x = 0) = \theta_t$, where θ_t is the angle of root rotation. Solving Eq. (A.2) with the boundary conditions, we obtain that

$$w(x) = \frac{P}{6EI}\left(x^3 + 3ax^2\right) - \left(\frac{P}{\kappa\mu A} + \theta_t\right)x. \tag{A.3}$$

Assuming linear elasticity, the angle of the root rotation depends linearly on the shear force and bending moment at $x = 0$:

$$\theta_t = c_1\frac{P}{Ehb} + c_2\frac{Pa}{Eh^2b} \tag{A.4}$$

where c_1 and c_2 are dimensionless coefficients. Using a finite element method (Yu and Hutchinson 2002; Mei et al. 2011), we calculated the coefficients and obtained: $c_1 = 2.6033$ and $c_2 = 8.0743$.

By (A.3), the opening of the DCB specimen at the loading point ($x = -a$) is

$$\begin{aligned} d &= 2w\,(x = -a) \\ &= \frac{2Pa^3}{3EI}\left[1 + \frac{c_2}{4}\frac{h}{a} + \left(\frac{1+\nu}{2\kappa} + \frac{c_1}{4}\right)\left(\frac{h}{a}\right)^2\right] \end{aligned} \tag{A.5}$$

The elastic strain energy in the DCB specimen is

$$\begin{aligned} U(a) &= \frac{1}{2}Pd \\ &= \frac{P^2a^3}{3EI}\left[1 + \frac{c_2}{4}\frac{h}{a} + \left(\frac{1+\nu}{2\kappa} + \frac{c_1}{4}\right)\left(\frac{h}{a}\right)^2\right]. \end{aligned} \tag{A.6}$$

The energy release rate for the crack growth is then obtained as

$$\begin{aligned} J &= \frac{1}{b}\frac{dU}{da} \\ &= \frac{12P^2a^2}{Eh^3b^2}\left[1 + \frac{c_2}{6}\frac{h}{a} + \left(\frac{1+\nu}{6\kappa} + \frac{c_1}{12}\right)\left(\frac{h}{a}\right)^2\right] \end{aligned} \tag{A.7}$$

With $\nu = 0.22$ for silicon, Eq. (A.7) becomes

$$J = \frac{12P^2a^2}{Eh^3b^2}\left(1 + 1.346\frac{h}{a} + 0.461\left(\frac{h}{a}\right)^2\right) \tag{A.8}$$

which compares closely with Eq. (10). With (A.5), we obtained the energy release rate in terms of the opening displacement at the loading point as given in Eq. (11).

We note that, if the angle of root rotation is taken to be zero by setting $c_1 = c_2 = 0$, the energy release rate in (A.7) becomes

$$J = \frac{12P^2a^2}{Eh^3b^2}\left[1 + \left(\frac{1+\nu}{6\kappa}\right)\left(\frac{h}{a}\right)^2\right] \tag{A.9}$$

A comparison between (A.7) and (A.9) suggests that the effect of root rotation (scaling with h/a) is more significant than the effect of shear.

Appendix B: An analytical model for DCB specimen

An analytical approach is presented here by combining simple beam theory (neglecting the shear effect) with a cohesive zone model, which is similar to a previous work by Stigh (1988) but is specifically formulated for

the wedge-loaded DCB test. By symmetry, only the top beam is considered (Fig. 8c). The deflection of the beam is governed by the simple beam equation,

$$EI\frac{d^4w}{dx^4} = -q, \tag{B.1}$$

where q is the intensity of the distributed load (force per unit length) acting on the beam. As shown in Fig. 8c, for a DCB specimen with a crack of length a (measured from the loading point to the crack tip), the interfacial load intensity can be specified in two regions. First, for $x < 0$, where the interface has been fully fractured, we have zero load intensity ($q = 0$) except at the loading point ($x = -a$). Ahead of the crack tip ($x > 0$), a cohesive zone develops as the crack opens up, where the load intensity depends on the traction-separation relation of the interface, i.e., $q = b\sigma(\delta)$, noting that $\delta = 2w$ for DCB.

To be specific, we consider the bilinear traction-separation law as sketched in Fig. 7a. The problem is solved in two steps. First, starting from a virgin DCB specimen with an initial crack, as the crack opens up, the interface opens elastically until the crack tip opening displacement (CTOD) reaches the critical value (δ_0) for damage initiation. The CTOD is simply twice the deflection at $x = 0$, i.e., $\delta^* = 2w\,(0)$. Next, when $\delta^* > \delta_0$, a damage zone develops ahead of the crack tip. For the wedge-loaded DCB specimen, the crack length a first decreases as the wedge is pushed towards the crack tip, until the CTOD reaches δ_c. Subsequently, as the wedge is advanced further, the crack grows in a steady state manner with a constant crack length.

Solving Eq. (B.1) for $-a < x < 0$ along with the boundary conditions, we obtain the normal crack opening displacement (NCOD):

$$\delta(x) = \delta^* - \theta^* x + \frac{Pa^3}{3EI}\left[3\left(\frac{x}{a}\right)^2 + \left(\frac{x}{a}\right)^3\right], \tag{B.2}$$

where θ^* the crack-tip opening angle (CTOA), which is twice of the angle of root rotation for each beam. The opening displacement at the loading point ($x = -a$) is thus

$$d = \frac{2Pa^3}{3EI} + \theta^* a + \delta^*. \tag{B.3}$$

We note that, while Eqs. (B.2) and (B.3) are independent of any specific traction-separation relation for the interface, the CTOD (δ^*) and CTOA (θ^*) both depend on the interfacial properties as discussed below.

Elastic opening of the interface

When $\delta^* < \delta_0$, the interface ahead of the crack tip ($x > 0$) remains in the elastic regime and the load intensity is simply, $q = 2bK_0w$, by the bilinear traction-separation relation. The beam equation (B.1) becomes

$$\frac{d^4w}{dx^4} + \frac{2K_0b}{EI}w = 0. \tag{B.4}$$

Assume that the beam is infinitely long, with zero deflection and rotation at infinity ($x \to \infty$). Along with the boundary conditions at the crack tip ($x = 0$), we solve Eq. (B.4) and obtain that, for $x > 0$,

$$\delta(x) = \delta^* e^{-\lambda x}\left(\cos(\lambda x) + \left(1 - \frac{\theta^*}{\lambda\delta^*}\right)\sin(\lambda x)\right), \tag{B.5}$$

where $\lambda = \left(\frac{6K_0}{Eh^3}\right)^{1/4}$.

To find the CTOD and CTOA, we apply the continuity conditions for the bending moment and shear force at $x = 0$, which leads to

$$-\lambda^2\delta^*\left(1 - \frac{\theta^*}{\lambda\delta^*}\right) = \frac{Pa}{EI}, \tag{B.6}$$

$$\lambda^3\delta^*\left(2 - \frac{\theta^*}{\lambda\delta^*}\right) = \frac{P}{EI}. \tag{B.7}$$

Solving Eqs. (B.6) and (B.7) simultaneously, we obtain that

$$\delta^* = \frac{P}{\lambda^3 EI}(\lambda a + 1), \tag{B.8}$$

$$\theta^* = \frac{P}{\lambda^2 EI}(2\lambda a + 1). \tag{B.9}$$

Inserting (B.8) and (B.9) into Eq. (B.3), we obtain the opening displacement at the loading point as

$$d = \frac{2Pa^3}{3EI}\left(1 + \frac{3}{\lambda a} + \frac{3}{(\lambda a)^2} + \frac{3}{2(\lambda a)^3}\right). \tag{B.10}$$

The elastic strain energy of the system (including 2 beams and the interface) equals the work done by the load P, namely

$$U(a) = \frac{1}{2}Pd = \frac{P^2a^3}{3EI}\left(1 + \frac{3}{\lambda a} + \frac{3}{(\lambda a)^2} + \frac{3}{2(\lambda a)^3}\right). \tag{B.11}$$

The corresponding energy release rate for crack growth is then obtained as

$$J = \frac{1}{b}\frac{dU}{da} = \frac{12P^2a^2}{Eb^2h^3}\left(1 + \frac{1}{\lambda a}\right)^2. \tag{B.12}$$

In terms of the loading displacement, the energy release rate is

$$J = \frac{3Eh^3d^2}{16a^4}\left(\frac{1+\frac{1}{\lambda a}}{1+\frac{3}{\lambda a}+\frac{3}{(\lambda a)^2}+\frac{3}{2(\lambda a)^3}}\right)^2. \quad \text{(B.13)}$$

The results in (B.12) and (B.13) are recast in Eqs. (12) and (13).

It can be shown that

$$\frac{dJ}{d\delta^*} = K_0\delta^*, \quad \text{(B.14)}$$

which recovers the elastic part of the bilinear traction-separation relation for $\delta^* < \delta_0$.

The critical load for damage initiation at the crack tip is obtained by setting $\delta^* = \delta_0$, which gives that

$$P_0(a) = \frac{\lambda^3 EI\delta_0}{\lambda a+1} \quad \text{(B.15)}$$

and

$$d_0(a) = \frac{2\lambda^3a^3\delta_0}{3(\lambda a+1)}\left(1+\frac{3}{\lambda a}+\frac{3}{(\lambda a)^2}+\frac{3}{2(\lambda a)^3}\right). \quad \text{(B.16)}$$

Correspondingly, the critical energy release rate is

$$J_0 = \frac{1}{2}\sigma_0\delta_0, \quad \text{(B.17)}$$

which is the triangular area underneath the linear elastic part of the traction-separation curve (Fig. 7a).

Crack opening with a damage zone

Next, when $\delta^* > \delta_0$, the traction along the interface is specified in two parts. Assume a damage zone of length c ahead of the crack tip. Within the damage zone ($0 < x < c$), the damage parameter as defined in Eq. (3) varies between 0 and 1, and the load intensity varies accordingly, i.e., $q = 2bK_0w(1-D)$. Beyond the damage zone ($x > c$), the interface is undamaged ($D = 0$) and remains elastic with $q = 2bK_0w$. For $0 < x < c$, the beam equation becomes

$$\frac{d^4w}{dx^4} + \frac{K_0b}{EI}\frac{\delta_0}{\delta_c-\delta_0}(\delta_c - 2w) = 0. \quad \text{(B.18)}$$

Solving Eq. (B.18), we obtain that,

$$w(x) = B_1\cosh(kx) + B_2\sinh(kx) + B_3\cos(kx) + B_4\sin(kx) + \frac{\delta_c}{2}, \quad \text{(B.19)}$$

where $k = \left(\frac{24K_0\delta_0}{Eh^3(\delta_c-\delta_0)}\right)^{\frac{1}{4}}$.

The NCOD for $x < 0$ is given in Eq. (B.2). At the crack tip ($x = 0$), we have the continuity conditions for the deflection, rotation, bending moment, and shear force, which lead to

$$B_1 + B_3 + \frac{\delta_c}{2} = \frac{\delta^*}{2}, \quad \text{(B.20)}$$

$$kB_2 + kB_4 = -\frac{\theta^*}{2}, \quad \text{(B.21)}$$

$$B_1 - B_3 = \frac{1}{k^2a^2}\frac{Pa^3}{EI}, \quad \text{(B.22)}$$

$$B_2 - B_4 = \frac{1}{k^3a^3}\frac{Pa^3}{EI}. \quad \text{(B.23)}$$

Solving (B.20)–(B.23), we obtain that

$$\begin{pmatrix}B_1\\B_2\\B_3\\B_4\end{pmatrix} = \frac{1}{2}\begin{bmatrix}1&0&1&0\\0&1&0&1\\1&0&-1&0\\0&1&0&-1\end{bmatrix}\begin{pmatrix}\frac{\delta^*-\delta_c}{2}\\-\frac{\theta^*}{2k}\\\frac{1}{k^2a^2}\frac{Pa^3}{EI}\\\frac{1}{k^3a^3}\frac{Pa^3}{EI}\end{pmatrix}. \quad \text{(B.24)}$$

For $x > c$, where the interface opens elastically, we solve Eq. (B.4) and obtain that,

$$w(x) = \frac{\delta_0}{2}e^{-\lambda(x-c)}\left(\cos\lambda(x-c) + \left(1-\frac{\theta_0}{\lambda\delta_0}\right)\sin\lambda(x-c)\right), \quad \text{(B.25)}$$

where θ_0 is the opening angle of the interface at ($x = c$), and the NCOD there has been set to be δ_0 according to the bilinear traction-separation relation.

The continuity conditions at $x = c$ require that

$$B_1\cosh(kc) + B_2\sinh(kc) + B_3\cos(kc) + B_4\sin(kc) + \frac{\delta_c}{2} = \frac{\delta_0}{2}, \quad \text{(B.26)}$$

$$kB_1\sinh(kc) + kB_2\cosh(kc) - kB_3\sin(kc) + kB_4\cos(kc) = -\frac{\theta_0}{2}, \quad \text{(B.27)}$$

$$k^2B_1\cosh(kc) + k^2B_2\sinh(kc) - k^2B_3\cos(kc) - k^2B_4\sin(kc) = -\lambda^2\delta_0\left(1-\frac{\theta_0}{\lambda\delta_0}\right), \quad \text{(B.28)}$$

$$k^3B_1\sinh(kc) + k^3B_2\cosh(kc) + k^3B_3\sin(kc) - k^3B_4\cos(kc) = \lambda^3\delta_0\left(2-\frac{\theta_0}{\lambda\delta_0}\right). \quad \text{(B.29)}$$

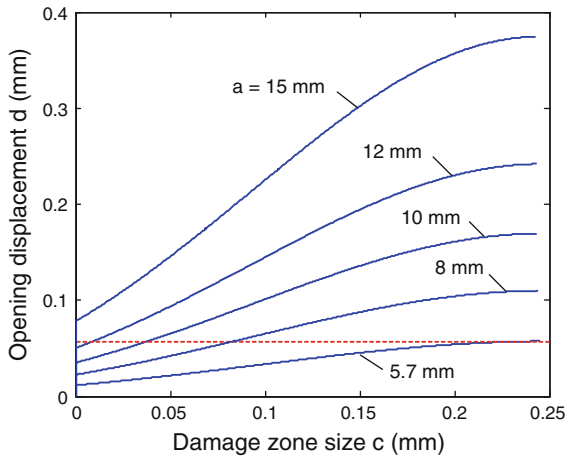

Fig. A1 Opening displacement at the loading point as a function of the damage zone size for different crack lengths, calculated based on the analytical model. The *horizontal dashed line* indicates the opening $d = 56.8\,\mu\text{m}$ for the wedge-loaded DCB specimen

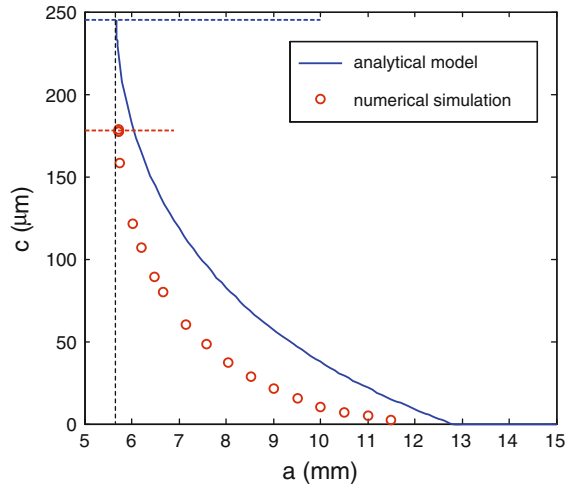

Fig. A2 The damage zone size as a function of the crack length for the wedge-loaded DCB specimen with $d = 56.8\,\mu\text{m}$, comparing the analytical solution with finite element simulation. The *horizontal lines* indicate the steady-state damage zone sizes, and the *vertical line* indicates the steady-state crack length

Inserting Eq. (B.24) into Eqs. (B.26)–(B.29), we obtain that

$$\begin{bmatrix} \Phi_{11} & \Phi_{12} & \Phi_{13} & 0 \\ \Phi_{21} & \Phi_{22} & \Phi_{23} & 1/2 \\ \Phi_{31} & \Phi_{32} & \Phi_{33} & -\lambda/k \\ \Phi_{41} & \Phi_{42} & \Phi_{43} & \lambda^2/k^2 \end{bmatrix} \begin{pmatrix} \frac{Pa^3}{EI} \\ \delta^* - \delta_c \\ \theta^*/k \\ \theta_0/k \end{pmatrix} = \begin{pmatrix} \frac{\delta_0 - \delta_c}{2} \\ 0 \\ -\lambda^2\delta_0/k^2 \\ 2\lambda^3\delta_0/k^3 \end{pmatrix}, \tag{B.30}$$

where

$$\begin{bmatrix} \Phi_{11} & \Phi_{12} & \Phi_{13} \\ \Phi_{21} & \Phi_{22} & \Phi_{23} \\ \Phi_{31} & \Phi_{32} & \Phi_{33} \\ \Phi_{41} & \Phi_{42} & \Phi_{43} \end{bmatrix} = \frac{1}{2} \begin{bmatrix} \cosh(kc) & \sinh(kc) & \cos(kc) & \sin(kc) \\ \sinh(kc) & \cosh(kc) & -\sin(kc) & \cos(kc) \\ \cosh(kc) & \sinh(kc) & -\cos(kc) & -\sin(kc) \\ \sinh(kc) & \cosh(kc) & \sin(kc) & -\cos(kc) \end{bmatrix} \tag{B.31}$$

$$\begin{bmatrix} 1 & 0 & 1 & 0 \\ 0 & 1 & 0 & 1 \\ 1 & 0 & -1 & 0 \\ 0 & 1 & 0 & -1 \end{bmatrix} \begin{bmatrix} 0 & \frac{1}{2} & 0 \\ 0 & 0 & -\frac{1}{2} \\ \frac{1}{k^2a^2} & 0 & 0 \\ \frac{1}{k^3a^3} & 0 & 0 \end{bmatrix}$$

Given the material properties of the elastic beam and the interface, we can solve Eq. (B.30) by linear algebra

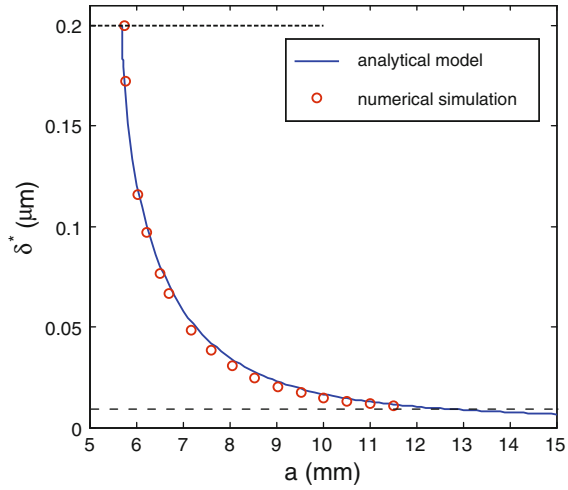

Fig. A3 CTOD as a function of the crack length for the wedge-loaded DCB specimen with $d = 56.8\,\mu\text{m}$. The *two horizontal lines* indicate the critical separations, $\delta_0 = 9$ nm and $\delta_c = 200$ nm, respectively

to obtain four unknown quantities: P, δ^*, θ^*, and θ_0, for a specific crack length a and damage zone size c. The opening displacement at the loading point can then be obtained as $d\,(a, c) = \frac{2Pa^3}{3EI} + \theta^* a + \delta^*$. Figure A1 plots the opening displacement as a function of the damage zone size c for different crack lengths. As expected, longer cracks and larger damage zones are produced by larger applied displacements. In order to apply this

analysis to the wedge test, the wedge thickness is taken to be the applied displacement i.e., $d\,(a, c) = h_w$ (see the dashed line in Fig. A1). Then the damage zone size for each crack length is determined by the intersections of the parametric curves with the dashed line. The results are shown in Fig. A2. For comparison, a finite element model of a bilayer DCB specimen was developed using cohesive elements with the bilinear traction-separation relation. The damage zone size from the analytical model was notably larger than that from the finite-element simulation. The discrepancy may be attributed to the shear effect that was neglected in the analytical model (Williams and Hadavinia 2002; Li et al. 2004).

The CTOD δ^* were obtained from the same solutions as a function of the crack length (Fig. A3). Interestingly, the solutions are in excellent agreement, which suggests the CTOD are insensitive to the shear effect.

The energy release rate for the wedge-loaded DCB specimen can be calculated by the J-integral over a contour around the crack tip and enclosing the entire cohesive zone, namely

$$J = -2\int_0^\infty \left(\sigma(x)\frac{dw}{dx}\right) dx. \tag{B.32}$$

Using the bilinear traction-separation relation, (B.32) leads to Eq. (14).

References

Bao G, Suo Z (1992) Remarks on crack-bridging concepts. Appl Mech Rev 45(8):355–366

Barenblatt GI (1962) The mathematical theory of equilibrium cracks in brittle fracture. Adv Appl Mech 7:55–129

Brantley WA (1973) Calculated elastic constants for stress problems associated with semiconductor devices. J Appl Phys 44(1):534–535

Chai YS, Liechti KM (1992) Asymmetric shielding in interfacial fracture under in-plane shear. J Appl Mech 59(2):295–304

Chow CL, Woo CW, Sykes JL (1979) On the determination and application of COD to epoxy-bonded aluminum joints. J Strain Anal Eng Des 14(2):37–42

Cox BN, Marshall DB (1991) The determination of crack bridging forces. Int J Frac 49(3):159–176

Dugdale DS (1960) Yielding of steel sheets containing slits. J Mech Phys Solids 8(2):100–104

Feraren P, Jensen HM (2004) Cohesive zone modelling of interface fracture near flaws in adhesive joints. Eng Fract Mech 71(15):2125–2142

Fichter WB (1983) The stress intensity factor for the double cantilever beam. Int J Frac 22(2):133–143

Gillis PP, Gilman JJ (1964) Double-Cantilever cleavage mode of crack propagation. J Appl Phys 35(3):647–658

Graff K (1975) Wave motion in elastic solids. Dover Publications Inc., New York

Hutchinson JW, Evans AG (2000) Mechanics of materials: top-down approaches to fracture. Acta Materialia 48(1):125–135

Hutchinson JW, Suo Z (1991) Mixed mode cracking in layered materials. Adv Appl Mech 29:64–191

Högberg JL, Sørensen BF, Stigh U (2007) Constitutive behaviour of mixed mode loaded adhesive layer. Int J Solids Struc 44(25-26):8335–8354

Kanninen MF (1973) An augmented double cantilever beam model for studying crack propagation and arrest. Int J Frac 9(1):83–92

Li S, Thouless MD (2006) Mixed-mode cohesive-zone models for fracture of an adhesively bonded polymer—matrix composite. Eng Fract Mech 73(1):64–78

Li S, Wang J, Thouless MD (2004) The effects of shear on delamination in layered materials. J Mech Phys Solids 52(1):193–214

Li S, Thouless MD, Waas AM, Schroeder JA, Zavattieri PD (2005) Use of mode-I cohesive-zone models to describe the fracture of an adhesively-bonded polymer-matrix composite. Compos Sci Technol 65(2):281–293

Liechti KM (1993) On the use of classical interferometry techniques in fracture mechanics. In: Epstein JS (ed) Experimental techniques in fracture III. VCH Publishers, New York, pp 95–124

Mei H, Gowrishankar S, Liechti KM, Huang R (2010) Initiation and propagation of interfacial delamination in integrated thin-film structures. In: Proceedings of 12th IEEE intersociety conference on thermal and thermomechanical phenomena in electronic systems (ITherm), pp 1–8. doi:10.1109/ITHERM.2010.5501290

Mei H (2011) Fracture and delamination of elastic thin films on compliant substrates: modeling and simulations. PhD Dissertation, The University of Texas at Austin.

Mei H, Landis CM, Huang R (2011) Concomitant wrinkling and buckle-delamination of elastic thin films on compliant substrates. Mech Mater 43(11):627–642

Mello AW, Liechti KM (2006) The effect of self-assembled monolayers on interfacial fracture. J Appl Mech 73(5):860–870

Mohammed I, Liechti KM (2000) Cohesive zone modeling of crack nucleation at bimaterial corners. J Mech Phys Solids 48(4):735–764

Moroni F, Pirondi A (2011) Cohesive zone model simulation of fatigue debonding along interfaces. Proc Eng 10:1829–1834

Parmigiani JP, Thouless MD (2007) The effects of cohesive strength and toughness on mixed-mode delamination of beam-like geometries. Eng Fract Mech 74(17):2675–2699

Shirani A, Liechti KM (1998) A calibrated frature process zone model for thin film blistering. Int J Fract 93:281–314

Sorensen L, Botsis J, Gmür Th, Humbert L (2008) Bridging tractions in mode I delamination: measurements and simulations. Compos Sci Technol 68(12):2350–2358

Stigh U (1988) Damage and crack growth analysis of the double cantilever beam specimen. Int J Fract 37(1):R13–R18

Stigh U, Andersson T (2000) An experimental method to determine the complete stress-elongation relation for a structural

adhesive layer loaded in peel. In: Williams JG, Pavan A (eds) Proceedings of the 2nd ESIS TC4 conference on the fracture of polymers, composites and adhesives in les diablerets, vol 27, ESIS publication, Switzerland Sept 1999, pp. 297–306.

Swadener JG, Liechti KM (1998) Asymmetric shielding mechanisms in the mixed-mode fracture of a glass/epoxy interface. J Appl Mech 65(1):25–29

Swadener JG, Liechti KM, Lozanne A (1999) The intrinsic toughness and adhesion mechanisms of a glass/epoxy interface. J Mech Phys Solids 47(2):223–258

Sørensen BF, Jacobsen TK (2003) Determination of cohesive laws by the J integral approach. Eng Fract Mech 70(14):1841–1858

Sørensen BF, Kirkegaard P (2006) Determination of mixed mode cohesive laws. Eng Fract Mech 73(17):2642–2661

Tvergaard V, Hutchinson JW (1992) The relation between crack growth resistance and fracture process parameters in elastic-plastic solids. J Mech Phys Solids 40(6):1377–1397

Valoroso N, Champaney L (2006) A damage-mechanics-based approach for modelling decohesion in adhesively bonded assemblies. Eng Fract Mech 73(18):2774–2801

Wiederhorn SM, Shorb AM, Moses RL (1968) Critical analysis of the theory of the double cantilever method of measuring fracture-surface energies. J Appl Phys 39(3):1569–1572

Williams JG (1989) End corrections for orthotropic DCB specimens. Compos Sci Technol 35(4):367–376

Williams JG, Hadavinia H (2002) Analytical solutions for cohesive zone models. J Mech Phys Solids 50(4):809–825

Yu HH, Hutchinson JW (2002) Influence of substrate compliance on buckling delamination of thin films. Int J Fract 113(1):39–55

Zhu Y, Liechti KM, Ravi-Chandar K (2009) Direct extraction of rate-dependent traction–separation laws for polyurea/steel interfaces. Int J Solids Struct 46(1):31–51